APPLIED PHYSICS

Multienergy x-ray detection and imaging enabled by working voltage regulating unipolar carrier collection in perovskite detectors

Yuwei Li[1], Xin Wang[1], Yijing Ding[1], Jingda Zhao[1], Shilin Liu[1], Yubing Xu[1], Qi Cheng[1], Ziyu Wei[1], Damian Chinedu Onwudiwe[2], Byung Seong Bae[3], Mehmet Ertuğrul [4], Ying Zhu[5], Wenbo Ma[6], Yang (Michael) Yang[6]*, Wei Lei[1]*, Xiaobao Xu[1]*

Multienergy x-ray imaging can provide additional substance information beyond morphology in conventional energy-integration imaging. The predominant approach, single photon counting, sets stringent requirements on low x-ray flux and signal discrimination and prolongs imaging time. Here, we report on the design of unipolar n-i-n perovskite detectors for multienergy x-ray imaging. Systematic characterization validates electrons dominating carrier dynamics in detectors, and the distribution of generated electrons varies as x-ray energy along its penetrating direction, whereas working voltage can manipulate electron drift length, ensuring their selective collection for x-ray energy discrimination. Our multienergy imaging array adopts high-flux x-ray in a normal imaging system and realizes fast 4-energy-bins x-ray images. By introducing the $\sigma(E_i)/\sigma(E_j)$-related multienergy digital subtraction algorithm, the images successfully distinguish the substance of targets side by side or by stacking, representing a notable advancement over conventional energy-integration imaging technique.

INTRODUCTION

Since 1895, x-ray detection and imaging have been extensively used in medical diagnosis, nondestructive testing, security checks, scientific research, etc. (*1*–*5*) In general, the detection of x-ray usually adopts the charge-integrating mode following Lambert's law $I(E_i) = I_0(E_i)e^{-\sigma(E_i)d}$ (I is the intensity of x-ray, σ is the substance-related x-ray attenuation coefficient, d is the thickness along the x-ray penetrating direction, and E_i denotes x-ray energies). Then, I determines the working current in detectors and thereafter the gray contrast in target imaging. Because both the σ and d have an influence on I, normal x-ray images mainly present the shape of the inspected sample. Although the computerized tomography can acquire the cross section or three-dimensional target imaging, it remains as before, focusing on the contrast and shape feature.

Energy-resolving capability is considered a critical feature for the next generation of x-ray imaging technologies due to its potential to greatly enhance material discrimination. In the past two decades, dual-energy x-ray detection has come into practical application by using stacked detectors or fast-switching x-ray sources (*6*–*8*). It shows the advances in diagnosing vascular disease and bone mineral density (*9*). However, it faces challenges with high radiation and image alignment in sequential scans, and its 2-energy bins are inadequate for complex material analysis. The photon counting has garnered intense attention for energy-resolved x-ray sensing and imaging (*4*, *5*, *10*). However, these detectors require a low x-ray flux to accurately identify individual photons and avoid the "pileup" effect, which, in turn, prolongs the imaging process. Furthermore, growing spectroscopic-grade and large-scale single crystals such as CdZnTe is extremely challenging and expensive.

Cost-effective lead halide perovskites have emerged as materials with superior properties for x-ray sensing, including superior x-ray absorption and a high $\mu\tau$ product (*3*, *11*–*21*), advancing both direct and indirect detectors (*2*, *15*, *17*, *22*–*30*). Their versatility in composition and carrier characteristics has driven the development of multienergy x-ray detection (*20*, *30*–*33*). Efforts include multilayer scintillator detectors and vertical matrix detectors with multielectrodes for depth-controlled carrier collection (*23*, *31*, *34*). However, indirect detectors based on scintillators are generally less efficient, and scaling multielectrode vertical detectors to create high-density pixel arrays presents inevitable fabrication challenges due to the complexity of the electrode integration process (*35*).

This study aims to develop simple, two-terminal, multienergy direct x-ray detectors and arrays, bypassing photon counting process. A unipolar n-i-n detector is introduced, using a Bi-$MAPbBr_3$(n)/$MAPbBr_3$(i)/Bi-$MAPbBr_3$(n) structure with $\mu_e\tau$ being two magnitude larger than $\mu_h\tau$ (*7*, *36*–*39*). As the depth of generated electrons varies with x-ray energy, the unipolar design enables precise regulation of electron drift length and collection by adjusting the applied working voltage. Subsequently, a simple yet effective algorithm was developed to decouple the information of x-ray energy by analyzing the output current at different voltages. The resulting 320-unit, 16-cm imaging array produces 4-energy-bins multispectral images in 20 s using normal x-ray sources (not synchrotron radiation sources). With our customized $\sigma(E_i)/\sigma(E_j)$-related multienergy digital subtraction algorithm, these multienergy x-ray images mitigate the impact of thickness variations, thereby providing morphological and material information for objects in adjacent or stacked configurations.

RESULTS

The imaging objects composed of different substances with certain thickness can produce similar image contrast in conventional energy-integration x-ray imaging (digital radiography, computed tomography,

[1]School of Electronic Science and Engineering, Southeast University, Nanjing, Jiangsu, China. [2]Department of Chemistry, School of Mathematics and Physical Sciences Faculty of Natural and Agricultural Sciences North-West University, Mafikeng Campus, Private Bag X2046, Mmabatho 2735, South Africa. [3]Department of Electronics & Display Engineering, Hoseo University, Hoseo Ro 79, Asan, Chungnam 31499, Republic of Korea. [4]Faculty of Engineering, Metallurgical and Materials Engineering, Karadeniz Technical University, Trabzon, Türkiye. [5]E-xray Electronic Co. Ltd., Suzhou, China. [6]College of Optical Science and Engineering, Zhejiang University, Hangzhou, Zhejiang 310027, China.
*Corresponding author. Email: xiaobaoxu@seu.edu.cn (X.X.); lw@seu.edu.cn (W.L.); yangyang15@zju.edu.cn (Y.Y.)

etc.) (*1*, *4*, *6*, *10*, *40*), which is the key limiting factor compared to energy-resolved x-ray detectors. According to Lambert's law, the penetrating depth of x-ray in detectors varies with its energy; low-energy x-rays are deposited near the surface, whereas high-energy x-rays penetrate more deeply. The discrimination of electrical signals generated at different positions within a detector allows for the resolution of x-ray energy (*31*). Figure 1 (A and B) illustrates the charge carrier dynamics in the direct x-ray detector with p-i-n and n-i-n architectures, respectively. Upon the absorption of x-ray photons, the electron-hole pairs are generated and driven toward different electrodes under a working voltage. In p-i-n detectors, both electrons and holes contribute to the electrical signal in the external circuit, making it difficult to distinguish their individual contributions due to the trade-off in the distance to the electrodes. In contrast, n-i-n unipolar detectors, or similarly p-i-p detectors, allow only electrons (or holes in the case of p-i-p) to dominate the electrical signal. The impact of the electric field on the electron drift length suggests a practical method for using the working voltage to control electron collection, which, in turn, enables the resolution of x-ray energy.

To elucidate the operating principle of our proposed unipolar n-i-n detector, Fig. 1C presents the schematic diagram of relationship between carrier dynamics and x-ray energy. The electron shifting length can be mathematically expressed as

$$x_n = \frac{V_n \cdot \mu \cdot \tau}{L} \tag{1}$$

in which L is the thickness of device and x_n is the electron drift length under a working voltage of ~V_n. By applying Lambert's law, we can infer that the electron drift length x_n ($x_1 < x_2 < x_3 < x_4 \leq L$) under a voltage of V_i corresponds to the maximum penetrating distance of x-ray with energy of E_i ($E_1 < E_2 < E_3 < E_4$). Thus, the variation in current (J_n) can be expressed as

$$\Delta J_n - \Delta J_{(n-1)} = \sum m_i \left[I\left(E_i\right)_{n-1} - I\left(E_i\right)_n \right] \tag{2}$$

Here, m_i is a factor that accounts for the conversion of x-ray with energy of ~E_i and intensity of $I(E_i)$ into photocurrent. Notably, both the electron production under x-ray irradiation and electron collection efficiency would affect m_i. In brief, as the working voltage increases, the primary increase in photocurrent is attributed to the collection of additional electrons generated by higher-energy x-ray. This relationship can be simplified as

$$\Delta J\left(E_i\right) = m_i I_0\left(E_i\right) \tag{3}$$

By determining the factor of m_i, we can establish the mapping relationship between the response current and the x-ray energy (*1*, *6*, *8*–*10*). Figure S1 refers to the solving process of the formula under different working voltages.

Following our previous discussions, we have constructed a unipolar detector and its imaging array using an ~1.5-mm $MAPbBr_3$ single crystal sandwiched between two 100-μm liquid-phase epitaxial n-type Bi-doped $MAPbBr_3$ (Bi-$MAPbBr_3$) (*21*, *37*). Tables S1 and S2

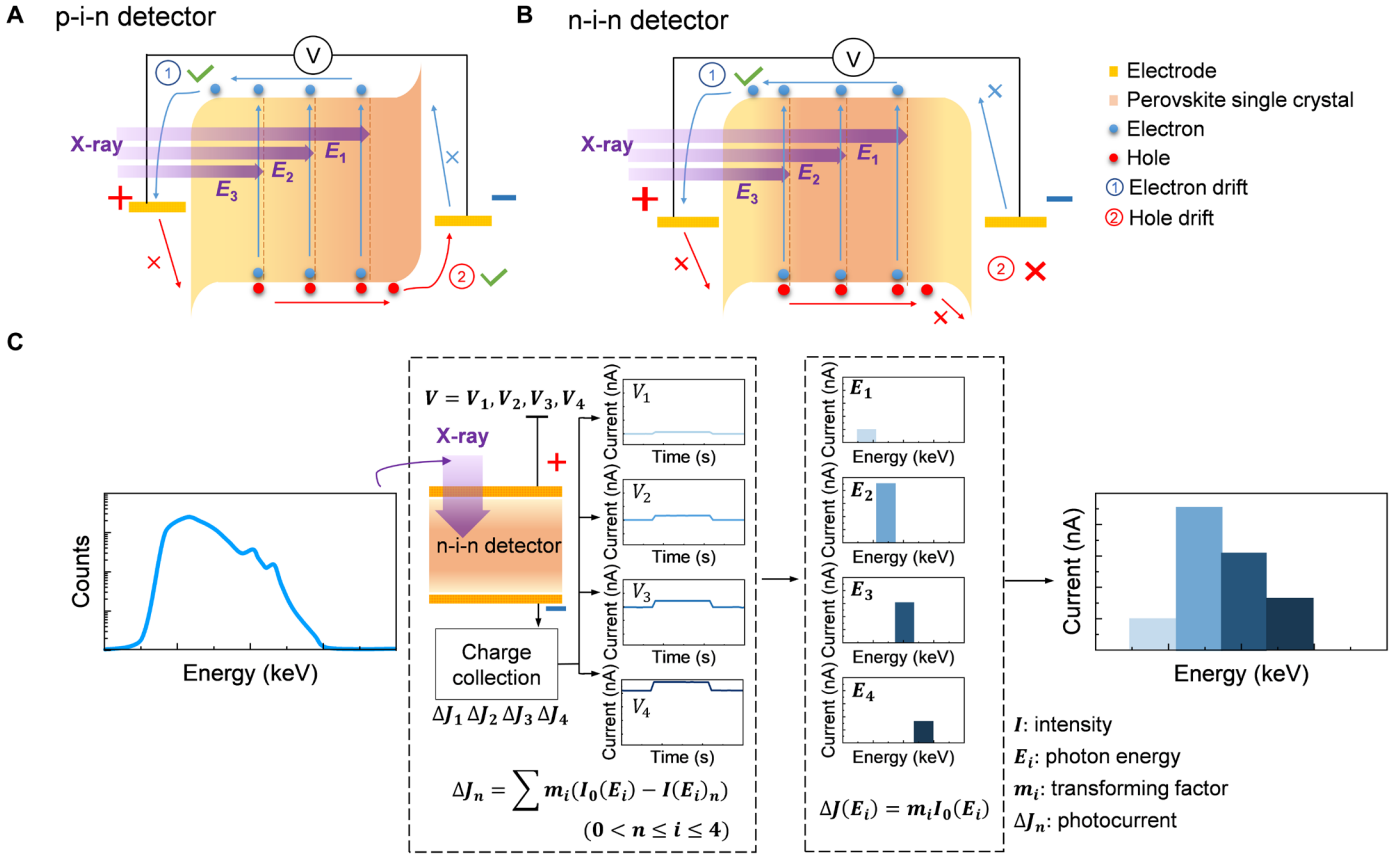

Fig. 1. Working mechanism of our proposed multienergy x-ray detector. Schematic diagrams of carrier dynamics in the x-ray detector with (**A**) a bipolar p-i-n structure, and (**B**) a unipolar n-i-n structure, and (**C**) the working mechanism for our proposed multienergy detection in the n-i-n detector.

provide the majority carrier concentration and characteristics of $MAPbBr_3$ and Bi-$MAPbBr_3$, respectively, as determined by Hall measurements. These measurements confirm that the Bi doping can convert $MAPbBr_3$ from a p-type to n-type semiconductor. The n-type characteristic of Bi-$MAPbBr_3$ ensures n-i-n architecture and that electrons dominate the device behavior (*30*, *36*).

Figure 2A illustrates the process of preparing our proposed multienergy x-ray linear array detector. To facilitate the signal readout, we use a process control block (PCB) board as the substrate. The $MAPbBr_3$ precursor, mixed with terpineol and ethyl cellulose, was used as adhesive for bonding the single crystal onto the PCB board (*41*) and was annealed at 85°C for ~20 min to promote its electrical contact.

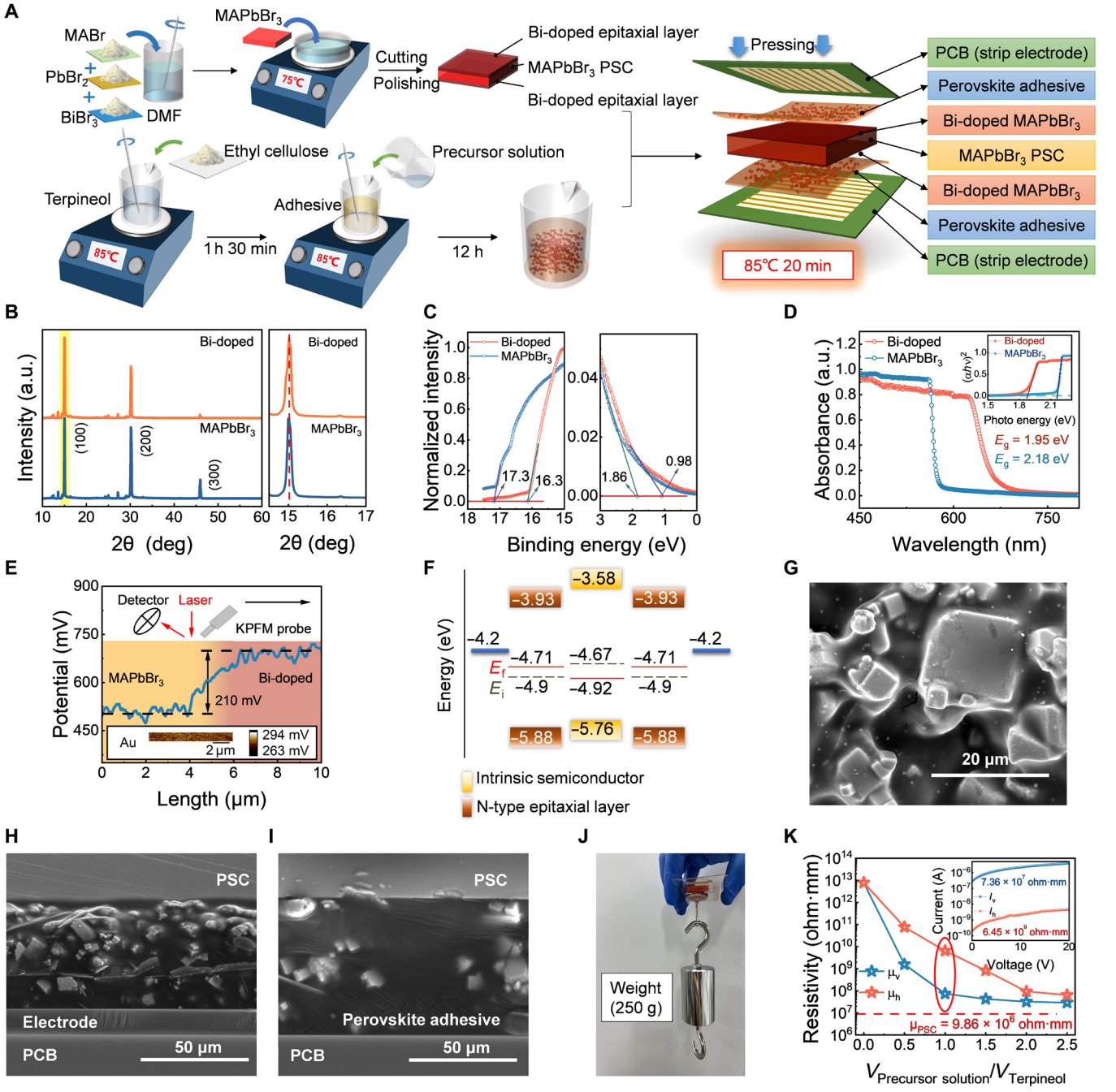

Fig. 2. Fabrication of the multienergy x-ray linear array detector. (**A**) Procedure for fabricating the perovskite single crystal and the n-i-n x-ray detector with Bi-$MAPbBr_3$/$MAPbBr_3$/Bi-$MAPbBr_3$, wherein the thickness of the $MAPbBr_3$ perovskite single crystal is 1.5 mm, the epitaxial Bi-$MAPbBr_3$ layer is 100 μm, and the thickness of perovskite adhesive is 80 μm. (**B**) XRD profile. a.u., arbitrary units; deg, degrees. (**C**) UPS. (**D**) Absorption of Bi-$MAPbBr_3$ and $MAPbBr_3$. (**E**) Kelvin probe force microscope (KPFM) of n-i-n structured devices at the n-i junction region. (**F**) Energy band diagram in the n-i-n detector. (**G**) SEM image of the dried perovskite adhesive paste. Cross-sectional SEM images of array sensing units on PCB with (**H**)/without metal strip electrodes (**I**). (**J**) Adhesion test of perovskite adhesives with 250 g weight. (**K**) Resistivity along the in-plane and out-plane direction.

Figure 2B presents the x-ray diffraction (XRD) profiles of the $MAPbBr_3$ and Bi- $MAPbBr_3$. No obvious shift in peaks occurs. The sharp characteristic peaks confirm their high crystallinity and purity. Ultraviolet photoelectron spectroscopy (UPS) measurements reveal the valence band (VB) of 5.76 and 5.88 eV for $MAPbBr_3$ and Bi-$MAPbBr_3$ crystals, respectively (Fig. 2C). Meanwhile, the absorption edge shifts from ~569 to ~636 nm, which indicates that the Bi doping narrows the bandgap from 2.18 to 1.95 eV (Fig. 2D). It is assumed that Bi doping introduces additional energy levels (*37*). Kelvin probe measurement implies that Bi doping results in a 0.21-V upshift in the surface potential (Fig. 2E). Together with UPS and absorption measurement, it verifies that the Bi doping induces a distinct n-type behavior in $MAPbBr_3$. Figure 2F depicts the energy level in the n-i-n unipolar detector. It promises electron transport in the whole device while the hole is blocked. The time-resolved photoluminescence confirms the electrons can be quickly extracted from $MAPbBr_3$ to Bi-$MAPbBr_3$ (fig. S2). It is worth noting that the n-i-n architecture can further suppress the leakage current.

The $MAPbBr_3$ paste is crucial for establishing the electric contact between the single crystal and PCB. Here, we found an optimized recipe, in which 10 ml of the $MAPbBr_3$ precursor [*N*,*N*′-dimethylformamide (DMF) with 12% $BiBr_2$] was mixed with ethyl cellulose solution (3 g in terpineol) in 1:1 (v/v). Figure 2G presents a top-view scanning electron microscopy (SEM) image of the dried paste, showing the presence of $MAPbBr_3$ microcrystals. The random size distribution of $MAPbBr_3$ powder is beneficial for good electrical contact. Figure S3 (A to E) gives the SEM images of paste with different mixing ratios, in which the shape and features of $MAPbBr_3$ crystals vary with the ratio. Figure 2 (H and I) shows the cross-sectional SEM images of sensing units in imaging array on the PCB, with and without strip metal electrodes, respectively. The perovskite grains within the paste are densely packed, forming a good conductive path for electrons. Figure 2J presents the adhesion test results. Even under a weight of 250 g, a tight bond is maintained. The conductivity of the paste shows an anisotropic behavior, with a resistivity of 6.45×10^9 ohm·mm in the out-of-plane direction and 7.36×10^7 ohm·mm in the in-plane direction (Fig. 2K). This feature ensures the efficient collection of charge carriers in the devices and suppresses the signal cross-talk among units.

To further confirm the unipolar character of sensing units in the array, we measured the carrier mobility in the detector units using the time-of-flight (ToF) (*41*) method as follows

$$\mu = \frac{d^2}{V \cdot t_\tau} \tag{4}$$

where V is the applied voltage and t_τ is the drifting time. The electron mobility (μ_e) is found to be ~114.41 $cm^2\ V^{-1}\ s^{-1}$ (Fig. 3A), whereas the hole mobility (μ_h) is determined to be 1.88 $cm^2\ V^{-1}\ s^{-1}$ (Fig. 3B). The two orders of magnitude difference in mobility values provides clear evidence of the unipolar character of the device, with electrons dominating the carrier behavior. For a comparison, the single crystal $MAPbBr_3$ device exhibits an electron mobility of 87.8 $cm^2\ V^{-1}\ s^{-1}$ (fig. S4A) and a hole mobility of 95.8 $cm^2\ V^{-1}\ s^{-1}$ (fig. S4B).

To evaluate the performance of sensing units, we conducted systematic characterizations, including the limit of detection (LoD), response rate, and sensitivity (*18*). By varying the x-ray dose rate, the sensing unit demonstrates a linear response from 2.7 to 58.6 $\mu Gy_{air}\ s^{-1}$ (Fig. 3C). Table S3 provides detailed information about the x-ray source used in tests. Following the IUPAC definition, we applied the signal-to-noise ratio (SNR) of 3 as the detectable limit and subsequently determined the LoD to be 81.2 $nGy_{air}\ s^{-1}$ under an electric field of 175 V cm^{-1}. This value is lower than the dose in computed tomography or digital subtraction angiography diagnosis imaging ensuring the safe x-ray imaging in the practical application (*42*). Figure S5A depicts the temporal response under different x-ray dose rates. The response shows a sharp on-and-off characteristic, with rise and fall times of ~176 and ~228 μs, respectively (Fig. 3D), indicating the potential for fast imaging in comparison to existing commercial detectors (table S4). Figure S5 (B and C) illustrates the effect of the electric field on the sensitivity. The sensitivity initially increases with electric field and then plateaus at 1.28×10^3 $\mu C\ Gy_{air}^{-1}\ cm^{-2}$ at an electric field of 175 V cm^{-1} (Fig. 3E). It proves that the applied electric field (working voltage) can manipulate the collection of charge carriers and, beyond 175 V cm^{-1}, the electric field's influence becomes negligible.

To further confirm the reliability of using work voltage to selectively collect charge carriers at different depths, we designed and conducted a measurement using a laser to induce the charge carriers at various depths (referring to fig. S6). As shown in Fig. 3F, the resulting currents correspond to the carrier collection. The efficient drift length of electrons increases as the working voltage increases. Consequently, the variation in current due to electron collection near the surface shows minimal change, whereas the primary enhancement in current is attributed to the collection of electrons from deeper depth within the $MAPbBr_3$. Under operational conditions (fig. S7), the simulated electric field within the device ensures unipolar carrier transport. This result confirms that the working voltage can regulate the carrier collection, establishing a crucial precondition for resolving the energy in x-ray.

Figure 3G presents the penetrating depth of x-rays with different energies, as simulated by Geant4 simulation (fig. S8 and table S5). The result confirms that the low-energy x-ray photons would deposit their energy near the surface, whereas high-energy x-ray photons penetrate more deeply. Figure 3H gives the photocurrent ratio to plastic, iron, and aluminum (Al) targets side by side under the electric field of 40, 100, 160, and 240 V cm^{-1} (fig. S9). The photocurrent ratio to different targets shows a noticeable irregular difference, which is fundamental for substance discrimination. Because the target size remains constant, the observed differences are attributed to the substance-specific attenuation coefficient [$\sigma(E_i)$]. It is worth noting that this data can only distinguish the difference in substance rather than recognition. Figure 3I shows the long-term operational stability of units in air, the performance only degraded by 8.7%.

Figure 4A presents the photograph of a multienergy imaging system, featuring an as-fabricated linear imaging array with 320 units spanning 16 cm. An enlarged view is provided in fig. S10. Figure 4B illustrates a quite uniformity of unit performance with a deviation of 8.5% in photocurrent across our array. The schematic diagram outlines the readout circuit and its operating logic, highlighting the amplifier, filter circuit, analog-to-digital conversion, and field programmable gate array (FPGA) as essential components. Further details on the signal readout and the noise are available in fig. S11. Under the operation of 600-kHz data acquisition at 10 V, the signal can be efficiently clarified from noise with SNR ~ 31.5. Under the continuous irradiation of an x-ray source (@80 kV, 4 mA), this imaging system can acquire over four pictures in 20 s, with each picture consisting of 320 × 300 pixels. The presence of an n-i junction in the detector can mitigate certain ion migrations, but it does not entirely eliminate their impact, particularly under x-ray irradiation. Notably, if the data acquisition time is reduced to 10 to 20 s (fig. S12), the attenuation of

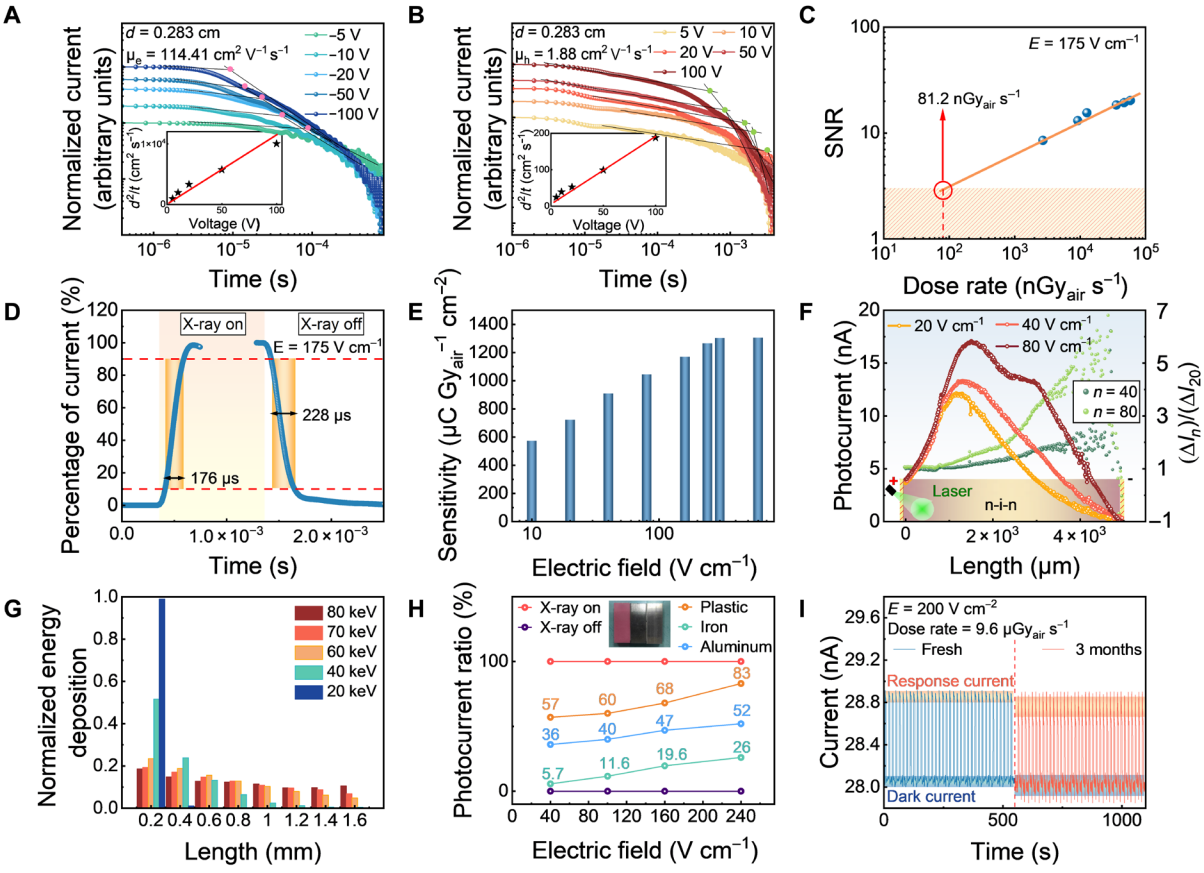

Fig. 3. Characterization of the n-i-n multienergy x-ray detector. (**A**) Electron mobility and (**B**) hole mobility in the n-i-n detector from the ToF method. (**C**) LoD in the n-i-n detector at an electric field of 175 V cm^{-1}. (**D**) Rising and falling time in the n-i-n detector at an electric field of 175 V cm^{-1}. (**E**) Sensitivity of the detector under different electric fields. (**F**) Result of the photocurrent with the position of laser irradiation under different electric field intensities. (**G**) Simulation results of the energy deposition ratio of x-ray photons with different energies at different depths of the detector. (**H**) Photocurrent ratio under different working electric field intensities toward plastic, iron, and Al sheets at an x-ray dose rate of 206.2 μGy$_{air}$ s^{-1}. (**I**) Response performance of the n-i-n detector stored in air for 3 months at room temperature.

photocurrent due to ion migration is small, ~0.3%. For an image with 256 gray levels, this results in a decrease of only 0.6 gray levels for the brightest pixel as gray levels are rounded to the nearest integer. Consequently, there is no perceptible change in gray level for imaging purposes. Therefore, provided that the data acquisition speed is sufficiently rapid, ion migration will have negligible effects on image quality.

Figure S13 establishes the mathematical foundation for discriminating material differences. Figure S14 illustrates side-by-side imaging targets of Al and polymethyl methacrylate (PMMA). The x-ray tubes are configured at 80 kV and 4 mA, as detailed in table S3. In normal x-ray imaging, Al and PMMA exhibit similar grayscale values (photocurrent). By applying operating voltages of 10 and 50 V, we obtain low-energy and high-energy x-ray imaging, respectively, as described in Eq. 3. Both images show an obvious contrast between Al and PMMA, especially in the low-energy image, confirming the advantage of distinguishing the objects side by side. For the high-density materials or thick materials, the contrast sometimes appears in the high-energy image.

To the best of our knowledge, conventional x-ray imaging struggles to differentiate between stacked targets, particularly when low-density materials are overlaid by high-density ones (*43*). Figure 4C presents the photograph of various imaging targets—Cu, Al, a layered sample of Al/PMMA/Cu, and PMMA—arranged from left to right, with a Cu cross serving as a positional reference. Figure 4D gives the obtained current response from sensing array under working voltages of 10 V (E_1), 20 V (E_2), and 50 V (E_4). Figure 4E contrasts the conventional and multienergy x-ray images. The conventional images display minimal variation in gray levels with changes in working voltage, but the multienergy images exhibit varying contrast ratios among targets. Notably, the low-density Al and PMMA are more discernible in the low-energy x-ray (E_1) images, whereas the high-density Cu stands out in the high-energy x-ray (E_4) images. To delineate the stacked samples layer by layer, we use the digital subtraction algorithm to obtain each layer in the stacked sample. According to fig. S13, we can get the $\sigma(E_i)/\sigma(E_j)$ in a single Cu layer, Al layer, and PMMA layer and then use $\sigma(E_i)/\sigma(E_j)$ as a silhouette coefficient to assign the correlation between the image signal and thickness of each layer in the stacked sample. The details of algorithm derivation can be found in Supplementary Discussion 11. As a result, in the stacked sample, each layer, even the PMMA and Al sheets under the Cu sheet, can be extracted separately. To enhance the visual difference, we use the pseudocolors for different substances. The result confirms the potential of unipolar sensing array in identifying the target under complicated surroundings with both substance and morphology information in imaging. Figure S15 displays a similar result with PMMA triangle under the Cu sheet.

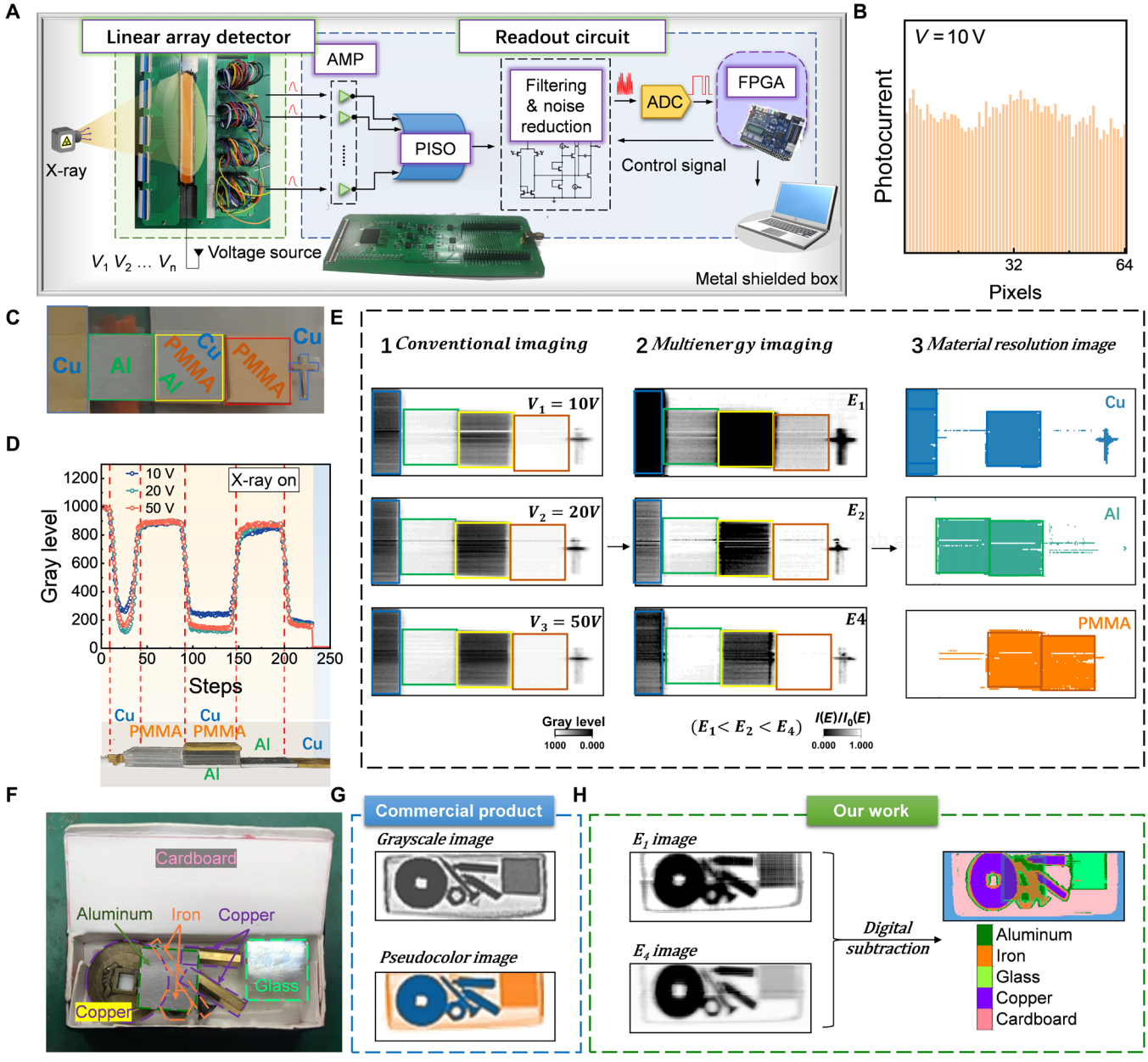

Fig. 4. Multienergy x-ray imaging with our multienergy x-ray detector array. (**A**) Photograph of the multienergy x-ray line imaging array with 320 n-i-n units in 16 cm and the schematic diagram of the readout system. (**B**) Uniformity of unit performance across the array. (**C**) Photograph of complicated imaging targets (the thickness of Cu is 1 mm, the thickness of PMMA is 3 mm, and the thickness of Al is 1 mm) and (**D**) their normalized response in a single n-i-n unit at different working voltages. (**E**) Procedure for material discrimination, where (1) represents the original x-ray images, (2) represents the reconstructed images of the object under different x-ray energies using algorithm, and (3) represents the result of material discrimination after energy silhouette. (**F**) Photograph of samples including Cu coin (2 mm), two Cu screws, Fe nut, Fe screw, Al sheet (1 mm), and glass block (5 mm) in a cardboard box, where the Al sheet is put on samples. (**G**) Gray image and pseudocolor image from a commercial security inspection machine. (**H**) Image from our multienergy sensing array.

To foster the imaging approach to the real-world scenario, we applied our unipolar sensing array to the complicated objects, as shown in Fig. 4F, where one Cu coin, two Cu screws, one Fe nut, one Fe screw, one Al sheet, and one glass block in a cardboard box. Although the Al sheet is obvious in the photograph, it is almost negligible in the x-ray image from the commercial x-ray imaging system (Fig. 4G). Even worse, in the commercial pseudocolor image, the Cu samples and Fe samples are ascribed to the same color. Figure 4H depicts the multienergy images from our imaging array under working voltages of 10 V (E_1), 20 V (E_2), 40 V (E_3), and 50 V (E_4); the Al sheet is slightly visible in the low-energy (E_1) x-ray image, and a difference between Cu samples and Fe samples is observed in the high-energy (E_4) x-ray image. Figure S16 shows the E_2 and E_3 images. Together with the $\sigma(E_i)/\sigma(E_j)$-related digital subtraction algorithm, we further explore the $\sigma(E_i)/\sigma(E_j)$ as a substance label. The discrimination of components in the cardboard box was successfully realized.

Figures S17 to S19 also show the application of our unipolar sensing array in discriminating the substances in various items, including chips, ancient coins, and sliding rheostat chains.

DISCUSSION

In this study, we have established a mechanism for multienergy x-ray detection, successfully implementing a multienergy n-i-n unipolar x-ray sensing array. We have elucidated its operational principle, with systematic characterizations confirming that electrons dominate the device behavior. This characteristic allows for the manipulation of carrier collection at various depths along the x-ray penetration path by adjusting the working voltage. Using a straightforward yet effective algorithm, we are able to deduce the x-ray energies from the output currents under different voltage conditions. With our customized $\sigma(E_i)/\sigma(E_j)$-related digital subtraction algorithm, our detector array effectively normalizes the impact of target thickness, demonstrating enhanced material discrimination capabilities over conventional energy-integration detectors.

MATERIALS AND METHODS

Materials

Anhydrous DMF and terpineol were purchased from Sinopharm. $PbBr_2$ (99.9%, 10031-22-8), CH_3NH_3Br (MABr, 99.9%, 6876-37-5), $BiBr_3$ (99.9%, 7787-58-8), and ethyl cellulose were purchased from Sigma-Aldrich. All chemicals were used without further purification.

Crystal growth procedure

The $MAPbBr_3$ single crystal was obtained through a solution-based heating crystallization method. The precursor solution was prepared by dissolving MABr in $PbBr_2$ with a molar ratio of 1:1 and a concentration of 1.3 M in a 600-ml DMF solution. After filtration, the precursor solution was transferred into a crystallization dish. Subsequently, the dish was placed in a water bath oven (AHX-871 SAFE OVEN CABINET) for heating crystallization, with the temperature gradually increased from 40° to 75°C at an increment of 1°C every 2 hours, followed by maintaining the current temperature for 4 hours. After ~1 week, we successfully obtained a large single crystal measuring 22 mm by 22 mm by 9 mm (fig. S20).

Perovskite adhesive preparation process

The ethyl cellulose was dissolved in terpineol at a temperature of 85°C, exhibiting a solubility of 0.3 g/ml, and stirred for a duration of 1 hour and 30 min. The perovskite precursor solution was subsequently introduced to the mixture of terpineol and ethyl cellulose at an equal volume ratio (1:1). The solution's temperature was maintained at 85°C while stirring for a period of 12 hours to obtain the perovskite viscous material. The resulting viscous material was heated and applied precisely to the desired adhesion site, ensuring firm adhesion upon cooling to room temperature.

Device fabrication

First, the $MAPbBr_3$ single crystal should be cut to the desired size using a cutting machine, followed by polishing the section to achieve a smooth surface. Next, 12% molar $BiBr_3$ should be added to the precursor solution and dissolved before filtering it and pouring it into a crystallization dish. The liquid-phase epitaxial growth method can then be used to epitaxially grow a Bi-doped n-type layer. The $MAPbBr_3$ single crystal should be placed in the precursor solution and heated to 75°C for 30 min, flipping it over halfway through for an additional 30 min of epitaxy. After completion of epitaxy, the crystal should be removed from the solution and its surface should be dried. A cutting machine should be used to remove any peripheral epitaxial layers, retaining only the upper and lower surfaces of the epitaxial layer. Last, the crystal should be affixed onto a PCB board using perovskite adhesive to obtain the detector.

Detector structure

The architecture of our detector is depicted in Fig. 2A. The x-ray absorption layer is composed of $MAPbBr_3$ and has a thickness of ~1.5 mm. The upper and lower surfaces of the absorption layer epitaxial a Bi-doped n-type layer, each about 0.1 mm thick. Outside the n-type layer is the perovskite adhesive layer, which is less than 0.1 mm thick, for bonding single crystals to PCB boards with patterned electrodes. The outermost layer is a patterned electrode PCB board, with copper serving as the electrode material. During all tests, x-rays enter the detector through the electrode surface. Initially, the detector structure was Cu/Bi-$MAPbBr_3$/$MAPbBr_3$/Bi-$MAPbBr_3$/Cu. Subsequently, to accommodate varying test requirements, some of the electrode materials were changed to indium tin oxide (ITO) (4.6 to 4.8 eV), which has a similar work function to copper (4.7 eV). Consequently, our detector now features three distinct structures based on different electrode materials: Cu/Bi-$MAPbBr_3$/$MAPbBr_3$/Bi-$MAPbBr_3$/Cu, ITO/Bi-$MAPbBr_3$/$MAPbBr_3$/Cu, and ITO/Bi-$MAPbBr_3$/$MAPbBr_3$/Bi-$MAPbBr_3$/ITO. Detectors with the structures Cu/Bi-$MAPbBr_3$/$MAPbBr_3$/Bi-$MAPbBr_3$/Cu and ITO/Bi-$MAPbBr_3$/$MAPbBr_3$/Cu are used for linear imaging. Meanwhile, detectors configured as ITO/Bi-$MAPbBr_3$/$MAPbBr_3$/Bi-$MAPbBr_3$/ITO are used for the electrical characterization of single-point detectors.

Detector performance measurement

To evaluate the detector's performance, a Keithley 6487 source meter was used to apply a bias voltage and record the resultant current. The x-ray detection performance was assessed using a PERLOVE medical chest x-ray machine (model PLX119C with a W target) as the x-ray source. Calibration of the dose rate was conducted using the Ray-safe Solo r/f dosimeter provided by PERLOVE Medical. The distance between the x-ray source and the detector is maintained at 50 cm. The dose rate of the x-ray is controlled by adjusting the tube voltage and tube current of the x-ray source (see table S3). All x-ray inspection–related measurements were performed in a light-tight test lead chamber, with the test equipment housed in a shielded metal box to minimize interference from ambient light and noise.

Imaging experiment procedure

The linear detector, along with its readout circuit and FPGA control circuit, was positioned directly beneath the x-ray source. A conveyor belt was placed between the x-ray source and the detector to transport the object under examination. Upon initiating x-ray imaging, an adjustable voltage supply (MP6030D) provided the detector with a bias voltage. Once the system stabilized, the x-ray source was activated, and the conveyor belt moved the object at a constant speed along the positive direction of the X-axis. The readout circuit collected and stored the imaging data under this bias voltage. After 5 s, the conveyor reversed direction and moved at a constant speed along the negative direction of the x axis while the bias voltage was adjusted. The readout circuit then collected and stored the imaging data under the bias voltage. This process was repeated until imaging data were

obtained at four distinct bias voltages. Subsequently, the imaging data saved in txt format were processed using Python to generate the imaging result graph and the dataset in xlsx format (see movie S1).

Readout circuit design

The primary charge amplifier chip used in the readout circuit is Texas Instruments' AFE0064, whereas the principal analog-to-digital conversion chip used is Texas Instruments' adc121s051. In addition, the main control FPGA model implemented is Cyclone IV.

Supplementary Materials

The PDF file includes:

Supplementary Discussions S1 to S12
Figs. S1 to S20
Tables S1 to S5
Legend for movie S1

Other Supplementary Material for this manuscript includes the following:

Movie S1

REFERENCES AND NOTES

1. C. H. Mccollough, P. Rajiah, J. P. Bois, T. N. Winfree, R. E. Carter, K. Rajendran, E. E. Williamson, J. E. Thorne, S. Leng, Comparison of photon-counting detector and energy-integrating detector CT for visual estimation of coronary percent luminal stenosis. *Radiology* **309**, e230853 (2023).
2. H. Wu, Y. Ge, G. Niu, J. Tang, Metal halide perovskites for X-ray detection and imaging. *Matter* **4**, 144–163 (2021).
3. A. Jana, S. Cho, S. A. Patil, A. Meena, Y. Jo, V. G. Sree, Y. Park, H. Kim, H. Im, R. A. Taylor, Perovskite: Scintillators, direct detectors, and X-ray imagers. *Mater. Today* **55**, 110–136 (2022).
4. G. A. Prenosil, H. Sari, M. Fürstner, A. Afshar-Oromieh, K. Shi, A. Rominger, M. Hentschel, Performance characteristics of the biograph vision quadra PET/CT system with a long axial field of view using the NEMA NU 2-2018 standard. *J. Nucl. Med.* **63**, 476–484 (2022).
5. J. N. Ullom, D. A. Bennett, Review of superconducting transition-edge sensors for x-ray and gamma-ray spectroscopy. *Supercond. Sci. Technol.* **28**, 084003 (2015).
6. R. M. Lorente Ramos, J. Azpeitia Armán, N. Arévalo Galeano, A. Muñoz Hernández, J. M. Garcia Gómez, J. Gredilla Molinero, Dual energy X-ray absorptimetry: Fundamentals, methodology, and clinical applications. *Radiologia* **54**, 410–423 (2012).
7. T. Flohr, M. Petersilka, A. Henning, S. Ulzheimer, J. Ferda, B. Schmidt, Photon-counting CT review. *Phys. Med.* **79**, 126–136 (2020).
8. E. Maire, J. Y. Buffière, L. Salvo, J. J. Blandin, W. Ludwig, J. M. Létang, On the application of X-ray microtomography in the field of materials science. *Adv. Eng. Mater.* **3**, 539–546 (2001).
9. D. Wen, K. Nye, B. Zhou, R. C. Gilkeson, A. Gupta, S. Ranim, S. Couturier, D. L. Wilson, Enhanced coronary calcium visualization and detection from dual energy chest x-rays with sliding organ registration. *Comput. Med. Imaging Graph.* **64**, 12–21 (2018).
10. F. I. Baffour, K. N. Glazebrook, A. Ferrero, S. Leng, C. H. Mccollough, J. G. Fletcher, K. Rajendran, Photon-counting detector CT for musculoskeletal imaging: A clinical perspective. *AJR Am. J. Roentgenol.* **220**, 551–560 (2023).
11. H. Tsai, F. Liu, S. Shrestha, K. Fernando, S. Tretiak, B. Scott, D. T. Vo, J. Strzalka, W. Nie, A sensitive and robust thin-film x-ray detector using 2D layered perovskite diodes. *Sci. Adv.* **6**, eaay0815 (2020).
12. J. Peng, C. Q. Xia, Y. Xu, R. Li, L. Cui, J. K. Clegg, L. M. Herz, M. B. Johnston, Q. Lin, Crystallization of $CsPbBr_3$ single crystals in water for X-ray detection. *Nat. Commun.* **12**, 1531–1531 (2021).
13. Q. Chen, J. Wu, X. Ou, B. Huang, J. Almutlaq, A. A. Zhumekenov, X. Guan, S. Han, L. Liang, Z. Yi, J. Li, X. Xie, Y. Wang, Y. Li, D. Fan, D. B. L. Teh, A. H. All, O. F. Mohammed, O. M. Bakr, T. Wu, M. Bettinelli, H. Yang, W. Huang, X. Liu, All-inorganic perovskite nanocrystal scintillators. *Nature* **561**, 88–93 (2018).
14. J. Jiang, M. Xiong, K. Fan, C. Bao, D. Xin, Z. Pan, L. Fei, H. Huang, L. Zhou, K. Yao, X. Zheng, L. Shen, F. Gao, Synergistic strain engineering of perovskite single crystals for highly stable and sensitive X-ray detectors with low-bias imaging and monitoring. *Nat. Photonics* **16**, 575–581 (2022).
15. R. Zhuang, X. Wang, W. Ma, Y. Wu, X. Chen, L. Tang, H. Zhu, J. Liu, L. Wu, W. Zhou, X. Liu, Y. M. Yang, Highly sensitive X-ray detector made of layered perovskite-like $(NH_4)_3Bi_2I_9$ single crystal with anisotropic response. *Nat. Photonics* **13**, 602–608 (2019).
16. Y. Zhang, Y. Liu, Z. Xu, H. Ye, Z. Yang, J. You, M. Liu, Y. He, M. G. Kanatzidis, S. Liu, Nucleation-controlled growth of superior lead-free perovskite $Cs_3Bi_2I_9$ single-crystals for high-performance X-ray detection. *Nat. Commun.* **11**, 2304 (2020).
17. K. R. Dudipala, T. H. Le, W. Nie, R. L. Z. Hoye, Halide perovskites and their derivatives for efficient, high-resolution direct radiation detection: Design strategies and applications. *Adv. Mater.* **36**, e2304523 (2024).
18. Y. Liu, Y. Zhang, X. Zhu, J. Feng, I. Spanopoulos, W. Ke, Y. He, X. Ren, Z. Yang, F. Xiao, K. Zhao, M. Kanatzidis, S. F. Liu, Triple-cation and mixed-halide perovskite single crystal for high-performance X-ray imaging. *Adv. Mater.* **33**, e2006010 (2021).
19. Y. Huang, L. Qiao, Y. Jiang, T. He, R. Long, F. Yang, L. Wang, X. Lei, M. Yuan, J. Chen, A-site cation engineering for highly efficient $MAPbI_3$ single-crystal X-ray detector. *Angew. Chem. Int. Ed. Engl.* **58**, 17834–17842 (2019).
20. Y. Shen, Y. Liu, H. Ye, Y. Zheng, Q. Wei, Y. Xia, Y. Chen, K. Zhao, W. Huang, S. F. Liu, Centimeter-sized single crystal of two-dimensional halide perovskites incorporating straight-chain symmetric diammonium Ion for X-ray detection. *Angew. Chem. Int. Ed. Engl.* **59**, 14896–14902 (2020).
21. X. Wang, Y. Pan, Y. Xu, J. Zhao, Y. Li, Q. Li, J. Chen, Z. Zhao, X. Zhang, B. S. Bae, D. C. Onwudiwe, X. Xu, W. Lei, Cascade perovskite single crystal for gamma-ray spectroscopy. *iScience* **26**, 107935 (2023).
22. Z. Li, F. Zhou, H. Yao, Z. Ci, Z. Yang, Z. Jin, Halide perovskites for high-performance X-ray detector. *Mater. Today* **48**, 155–175 (2021).
23. S. Deumel, A. van Breemen, G. Gelinck, B. Peeters, J. Maas, R. Verbeek, S. Shanmugam, H. Akkerman, E. Meulenkamp, J. E. Huerdler, M. Acharya, M. García-Batlle, O. Almora, A. Guerrero, G. Garcia-Belmonte, W. Heiss, O. Schmidt, S. F. Tedde, High-sensitivity high-resolution X-ray imaging with soft-sintered metal halide perovskites. *Nat. Electron.* **4**, 681–688 (2021).
24. Y. Liu, Z. Xu, Z. Yang, Y. Zhang, J. Cui, Y. He, H. Ye, K. Zhao, H. Sun, R. Lu, M. Liu, M. G. Kanatzidis, S. F. Liu, Inch-size 0D-structured lead-free perovskite single crystals for highly sensitive stable X-ray imaging. *Matter* **3**, 180–196 (2020).
25. Y. C. Kim, K. H. Kim, D.-Y. Son, D.-N. Jeong, J.-Y. Seo, Y. S. Choi, I. T. Han, S. Y. Lee, N.-G. Park, Printable organometallic perovskite enables large-area, low-dose X-ray imaging. *Nature* **550**, 87–91 (2017).
26. P. Jin, Y. Tang, D. Li, Y. Wang, P. Ran, C. Zhou, Y. Yuan, W. Zhu, T. Liu, K. Liang, C. Kuang, X. Liu, B. Zhu, Y. M. Yang, Realizing nearly-zero dark current and ultrahigh signal-to-noise ratio perovskite X-ray detector and image array by dark-current-shunting strategy. *Nat. Commun.* **14**, 626 (2023).
27. J. Zhao, L. Zhao, Y. Deng, X. Xiao, Z. Ni, S. Xu, J. Huang, Perovskite-filled membranes for flexible and large-area direct-conversion X-ray detector arrays. *Nat. Photonics* **14**, 612–617 (2020).
28. X. Song, Q. Cui, Y. Liu, Z. Xu, H. Cohen, C. Ma, Y. Fan, Y. Zhang, H. Ye, Z. Peng, R. Li, Y. Chen, J. Wang, H. Sun, Z. Yang, Z. Liu, Z. Yang, W. Huang, G. Hodes, S. F. Liu, K. Zhao, Metal-free halide perovskite single crystals with very long charge lifetimes for efficient X-ray imaging. *Adv. Mater.* **32**, e2003353 (2020).
29. Y. Zhou, J. Chen, O. M. Bakr, O. F. Mohammed, Metal halide perovskites for X-ray imaging scintillators and detectors. *ACS Energy Lett.* **6**, 739–768 (2021).
30. X. Wang, Y. Li, Y. Xu, Y. Pan, C. Zhu, D. Zhu, Y. Wu, G. Li, Q. Zhang, Q. Li, X. Zhang, J. Wu, J. Chen, W. Lei, Solution-processed halide perovskite single crystals with intrinsic compositional gradients for X-ray detection. *Chem. Mater.* **32**, 4973–4983 (2020).
31. J. Pang, S. Zhao, X. Du, H. Wu, G. Niu, J. Tang, Vertical matrix perovskite X-ray detector for effective multi-energy discrimination. *Light Sci. Appl.* **11**, 105 (2022).
32. P. Ran, L. Yang, T. Jiang, X. Xu, J. Hui, Y. Su, C. Kuang, X. Liu, Y. M. Yang, Multispectral large-panel X-ray imaging enabled by stacked metal halide scintillators. *Adv. Mater.* **34**, e2205458 (2022).
33. P. Zhang, Y. Hua, Y. Xu, Q. Sun, X. Li, F. Cui, L. Liu, Y. Bi, G. Zhang, X. Tao, Ultrasensitive and robust 120 keV hard X-ray imaging detector based on mixed-halide perovskite $CsPbBr_{3-n}I_n$ single crystals. *Adv. Mater.* **34**, e2106562 (2022).
34. X. Hu, S. Luo, J. Leng, C. Wang, Y. Chen, J. Chen, X. Li, H. Zeng, Density-discriminating chromatic x-ray imaging based on metal halide nanocrystal scintillators. *Sci. Adv.* **9**, eadh5081 (2023).
35. J. Miao, F. Zhang, Recent progress on highly sensitive perovskite photodetectors. *J. Mater. Chem. C* **7**, 1741–1791 (2019).
36. A. L. Abdelhady, M. I. Saidaminov, B. Murali, V. Adinolfi, O. Voznyy, K. Katsiev, E. Alarousu, R. Comin, I. Dursun, L. Sinatra, E. H. Sargent, O. F. Mohammed, O. M. Bakr, Heterovalent dopant incorporation for bandgap and type engineering of perovskite crystals. *J. Phys. Chem. Lett.* **7**, 295–301 (2016).
37. W. Tang, J. Zhang, S. Ratnasingham, F. Liscio, K. Chen, T. Liu, K. Wan, E. S. Galindez, E. Bilotti, M. Reece, M. Baxendale, S. Milita, M. A. Mclachlan, L. Su, O. Fenwick, Substitutional doping of hybrid organic-inorganic perovskite crystals for thermoelectrics. *J. Mater. Chem. A* **8**, 13594–13599 (2020).
38. Z. Zhang, L. Ren, H. Yan, S. Guo, S. Wang, M. Wang, K. Jin, Bandgap narrowing in Bi-doped $CH_3NH_3PbCl_3$ perovskite single crystals and thin films. *J. Phys. Chem. C* **121**, 17436–17441 (2017).
39. A. M. Ulatowski, A. D. Wright, B. Wenger, L. R. V. Buizza, S. G. Motti, H. J. Eggimann, K. J. Savill, J. Borchert, H. J. Snaith, M. B. Johnston, L. M. Herz, Charge-carrier trapping dynamics in bismuth-doped thin films of $MAPbBr_3$ perovskite. *J. Phys. Chem. Lett.* **11**, 3681–3688 (2020).

40. W. Zhang, H. Wang, H. Dong, F. Li, Z. Wang, Y. Shao, Mechanical polishing with chemical passivation of perovskite single crystals for high-performance X-ray detectors. *J. Mater. Chem. C* **10**, 17353–17363 (2022).
41. H. Wei, Y. Fang, P. Mulligan, W. Chuirazzi, H.-H. Fang, C. Wang, B. R. Ecker, Y. Gao, M. A. Loi, L. Cao, J. Huang, Sensitive X-ray detectors made of methylammonium lead tribromide perovskite single crystals. *Nat. Photonics* **10**, 333–339 (2016).
42. H. W. Goo, J. M. Goo, Dual-energy CT: New horizon in medical imaging. *Korean J. Radiol.* **18**, 555–569 (2017).
43. X. Ou, X. Chen, X. Xu, L. Xie, X. Chen, Z. Hong, H. Bai, X. Liu, Q. Chen, L. Li, H. Yang, Recent development in X-ray imaging technology: Future and challenges. *Research* **2021**, 2639–5274 (2021).

Acknowledgments
Funding: This work at Southeast University was financially supported by the NSFC (nos. T2322003, T2325020, 52172146, and 62175028), National Key Research and Development Program of China (2022YFE0139100), International cooperative research project of Jiangsu province (BZ2022008), and the Fundamental Research Funds for the Central Universities (no. 2242024K40017). **Author contributions:** W.L. and X.X. supervise this project. Y.L., with the help from Y.D., X.W., J.Z., S.L., Y.X., Q.C., and Z. W., carried out the experiments of materials, devices, and primal optical and electronic characterizations. Y.L. and X.X. prepared the manuscript with revisions from W.L., Y.Y., B.S.B., M.E., Y.Z., W.M. and D.C.O. All authors discussed the results and confirmed the manuscript. **Competing interests:** The authors declare that they have no competing interests. **Data and materials availability:** All data needed to evaluate the conclusions in the paper are present in the paper and/or the Supplementary Materials.

Submitted 6 August 2024
Accepted 20 June 2025
Published 23 July 2025
10.1126/sciadv.ads2995